Spatial model of convective solute transport in brain extracellular space does not support a "glymphatic" mechanism

Byung-Ju Jin,[1,2]* Alex J. Smith,[1,2]* and Alan S. Verkman[1,2]

[1]Department of Medicine and [2]Department of Physiology, University of California, San Francisco, San Francisco, CA 94143

A "glymphatic system," which involves convective fluid transport from para-arterial to paravenous cerebrospinal fluid through brain extracellular space (ECS), has been proposed to account for solute clearance in brain, and aquaporin-4 water channels in astrocyte endfeet may have a role in this process. Here, we investigate the major predictions of the glymphatic mechanism by modeling diffusive and convective transport in brain ECS and by solving the Navier–Stokes and convection–diffusion equations, using realistic ECS geometry for short-range transport between para-arterial and paravenous spaces. Major model parameters include para-arterial and paravenous pressures, ECS volume fraction, solute diffusion coefficient, and astrocyte foot-process water permeability. The model predicts solute accumulation and clearance from the ECS after a step change in solute concentration in para-arterial fluid. The principal and robust conclusions of the model are as follows: (a) significant convective transport requires a sustained pressure difference of several mmHg between the para-arterial and paravenous fluid and is not affected by pulsatile pressure fluctuations; (b) astrocyte endfoot water permeability does not substantially alter the rate of convective transport in ECS as the resistance to flow across endfeet is far greater than in the gaps surrounding them; and (c) diffusion (without convection) in the ECS is adequate to account for experimental transport studies in brain parenchyma. Therefore, our modeling results do not support a physiologically important role for local parenchymal convective flow in solute transport through brain ECS.

The Journal of General Physiology

INTRODUCTION

Transport of soluble macromolecules through the brain extracellular space (ECS), also called the interstitial space or parenchymal ECS, is facilitated by convection of cerebrospinal fluid (CSF) in the paravascular space (Ichimura et al., 1991; Weller et al., 2002; Abbott, 2004). More recently, a "glymphatic" mechanism has been proposed to mediate the clearance of solutes and macromolecules from the ECS, such as β-amyloid in neurodegenerative disease and metabolic waste during sleep, as well as to facilitate the distribution of nutrients to brain cells (Iliff et al., 2012; Jessen et al., 2015). In contrast to prior models, the glymphatic mechanism postulates that solute clearance in the ECS requires vectorial, advective flow of CSF from para-arterial to paravenous spaces though the brain parenchyma. As diagrammed in Fig. 1 A, advective flow entraps interstitial solutes in ECS fluid and enhances their clearance from brain tissue. The water permeability of astrocyte endfeet at the paravascular space/ECS interface and the ECS volume fraction in brain parenchyma have been proposed as important determinants of glymphatic flow (Iliff et al., 2012; Xie et al., 2013).

Glymphatic, advective flow in brain ECS represents a major departure from the generally accepted paradigm of diffusive solute transport in brain ECS. If correct, the glymphatic mechanism has broad implications to normal brain function, the neurophysiology of sleep, and the pathogenesis of neurodegeneration, stroke, edema, and other brain disorders. However, direct measurements of ECS fluid transport by photobleaching or tracer injection do not support directional movement of solutes in gray matter (Rosenberg et al., 1980; Papadopoulos et al., 2005) or in the paravascular space (Hladky and Barrand, 2014; Spector et al., 2015), and size-dependent penetration of CSF tracers into the brain parenchyma appears consistent with diffusive transport (Binder et al., 2004; Wolak and Thorne, 2013). It is also unclear how the water permeability of the astrocyte plasma membrane could influence advection of cell-impermeant solutes (Smith et al., 2015). We reasoned that an improved theoretical understanding of how variations in paravascular space hydrostatic pressure, ECS structure, and endfoot water permeability might alter advective flow in brain parenchyma would help to resolve some of the controversies surrounding the glymphatic hypothesis.

Prior theoretical work has modeled advective fluid dynamics in the paravascular space (Bilston et al., 2003; Schley et al., 2006; Wang and Olbricht, 2011; Coloma et al., 2016) and the effect of membrane water permeability on intracellular advective flow in astrocyte networks (Asgari et al., 2015); however, the effect of ECS geometry on advective movement of fluid and solutes between

*B.-J. Jin and A.J. Smith contributed equally to this paper.
Correspondence to Alan S. Verkman: Alan.Verkman@ucsf.edu
Abbreviations used: CSF, cerebrospinal fluid; ECS, extracellular space.

The Rockefeller University Press $30.00
J. Gen. Physiol. 2016 Vol. 148 No. 6 489–501
https://doi.org/10.1085/jgp.201611684

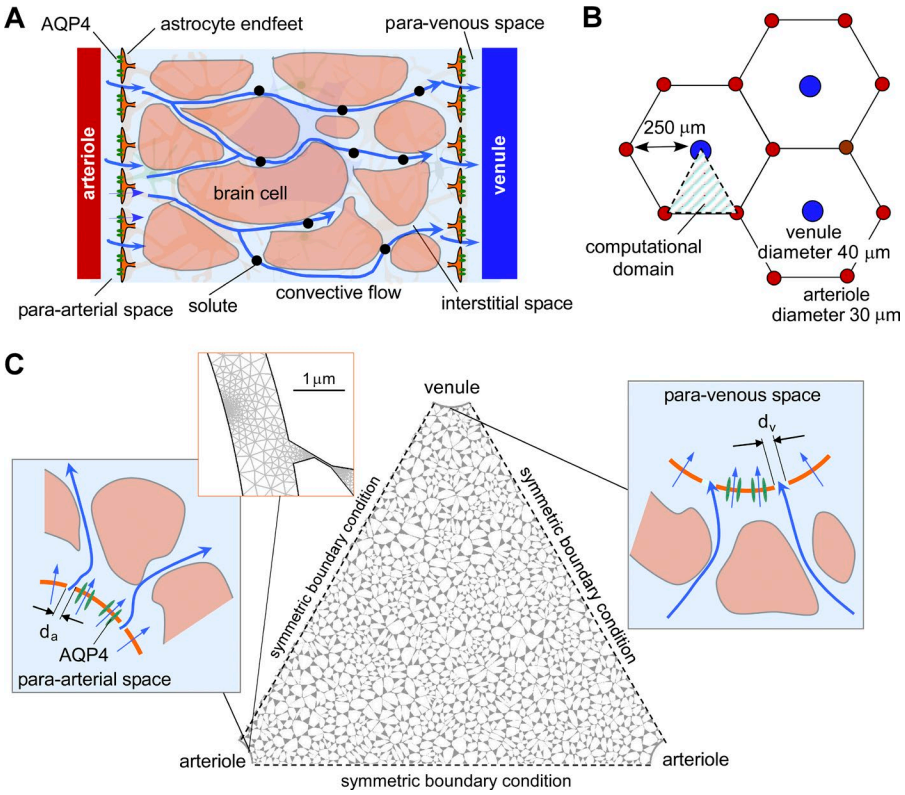

Figure 1. **Spatial model of convective fluid movement from para-arterial to paravenous spaces in brain ECS.** (A) Schematic showing the major features of the proposed glymphatic mechanism, including convective fluid movement from para-arterial to paravenous spaces through brain extracellular (interstitial) space. (B) Hexagonal spatial arrangement of arterioles and venules in brain parenchyma, showing triangular computational domain. (C) Diagram of water and solute movement between the para-arterial space and ECS, and the ECS and the paravenous space. d_a and d_v, gap distances between astrocyte endfeet in para-arterial and paravenous space.

the paravascular space and the ECS and through the ECS has not been explicitly modeled previously. Here, we developed a model of diffusion and advection in brain ECS that utilizes realistic paravascular and ECS geometry. Using the model, we determine the para-arterial/paravenous pressure difference required to drive significant ECS advection, quantify the role of astrocyte endfoot water permeability in ECS solute transport, and determine the adequacy of ECS diffusion to explain experimental data. The results provide a quantitative basis to understand advective transport mechanisms in the brain and suggest that purely diffusive transport in the parenchyma can explain existing experimental data.

MATERIALS AND METHODS

Model geometry

A model was developed to investigate short-range transport from paravascular to parenchymal spaces in the cerebral cortex where a pressure difference between the para-arterial and paravenous spaces could, in principle, drive advective fluid movement between these spaces (Fig. 1 A). We modeled advection–diffusion in brain ECS using paravascular and ECS geometries based on the cerebral cortex of primates where penetrating arterioles and ascending venules are arranged in a quasi-hexagonal configuration with an ∼2:1 ratio of arterioles/venules (Hirsch et al., 2012; Adams et al., 2015). Based on this anatomical information, the geometry of the microvascular lobule was idealized as a hexagonal lattice with a venule (Fig. 1 B; diameter 40 μm, blue circle) at the center, surrounded by six arterioles (diameter 30 μm, red circles). The distance between the venule and the arterioles was 250 μm (Adams et al., 2015). Exploiting symmetry, the computational domain was taken as a triangular region in the hexagonal lattice (Fig. 1 C). As arterioles and venules are arranged perpendicular to the cortical surface, a single two-dimensional slice provides a reasonable approximation of the three-dimensional volume, allowing for modeling of diffusion and advection in two dimensions.

A key feature of our model is the inclusion of specific, realistic geometry of the ECS rather than use of general porosity considerations. High-resolution three-dimensional reconstructions of brain neuropil that have been corrected for tissue shrinkage during fixation suggest that the ECS consists of an interconnected network of 40–80-nm-diameter tunnels connected by sheets of 10–40-nm width (Kinney et al., 2013). The interstitial space between the arterioles and venules in our model geometry was occupied with Voronoi cells, which recapitulate the structural heterogeneity in brain parenchyma (Hrabe et al., 2004; Jin et al., 2008). Seed points were initially positioned on a 5-μm square grid, which determines mean cell size. The seed points were displaced randomly in the x and y directions within a range of two-times larger than the mean cell size, which gives a Voronoi cell size distribution of 0.9–12.3 μm. Voronoi cell boundaries were eroded to create an interstitial space by trimming the corners of the cells and by short-

ening the edge of the cells to give specified ECS volume fraction α. This resulted in an ECS width of 10–100 nm (median ~60 nm). This geometry gave an effective hydraulic conductance of ~0.9×10^{-9} cm^4/dyne/s (Fig. S1), within the range of previous estimates (1.6×10^{-10} cm^4/dyne/s, Kaczmarek et al., 1997; $5 \times 10^{-9} cm^4$/dyne/s, Basser, 1992). To model different α values, changes in ECS width were proportional to the ECS volume change, $\Delta d_{ECS} \sim \Delta\alpha \times d_{ECS}{}^{o}$, where Δd_{ECS} is the ECS width change, $\Delta\alpha$ is the ECS volume change, and $d_{ECS}{}^{o}$ is the initial ECS width. The gaps between astrocyte endfeet surrounding the vessels were taken as 0.3% of astrocyte endfoot area (Mathiisen et al., 2010; 24-nm diameter spacing in the para-arterial space and 31 nm in the paravenous space).

Model parameter values/units

The model parameter values/units are as follows: P_f, astrocyte water permeability (0–0.4 cm/s); L_p, hydraulic conductance ($L_p = P_f/RT/v_w$), cm/(s·mmHg); v_W, partial molar volume of water (18 cm^3/mol); R, universal gas constant (62.4 mmHg·L/(mol·K)); T, absolute temperature (273°K); C_A and C_B, concentrations of solutes A (sum of all extracellular solutes; mM) and B (injected dye; μM); $C_A{}^o$, concentration of solute A in the para-arterial space (300 mM); $C_B{}^o$, concentration of solute B in the para-arterial space (10 μM); D_A, diffusion coefficient of solute A in the interstitial space (10^{-9} m^2/s; Goodman et al., 2005); D_B, diffusion coefficient of solute B in the interstitial space ($0.2–5 \times 10^{-10}$ m^2/s; Syková and Nicholson, 2008); ρ, fluid density (10^3 kg/m^3); μ, fluid dynamic viscosity (10^{-3} Pa·s); V, fluid velocity in the interstitial space (cm/s); P, pressure in the interstitial space (mmHg); P_a, pressure in the para-arterial space (0–10 mmHg); P_{amp}, amplitude of pulsatile pressure in the para-arterial space (0–100 mmHg); J_V, water transport through the astrocyte endfoot unit area (cm/s); J_A, solute A transport through the astrocyte endfoot gap (mol/(m·s)); J_B, solute B transport through the astrocyte endfoot gap (mol/(m·s)); and $J_A{}^{pump}$, solute A transport by active pumping through the astrocyte endfoot ($0–1.5 \times 10^{-3}$ mol/m^3).

Model computations

Modeling of advection–diffusion in a single two-dimensional microvascular lobule was implemented using COMSOL Multiphysics (COMSOL, version 3.4). The model is specified by advection–diffusion equations describing ion and fluorescent dye advection–diffusion,

$$\frac{\partial C_i}{\partial t} = \underbrace{-V \cdot \nabla C_i}_{\text{advection}} + \underbrace{D \nabla^2 C_i}_{\text{diffusion}},$$

where C_i is concentration of the i^{th} solute. The velocity field, V, was computed from the Navier–Stokes equation for an incompressible fluid and the continuity equation,

$$\rho \frac{\partial V}{\partial t} + \rho(V \cdot \nabla)V = -\nabla P + \mu \nabla^2 V$$

$$\nabla \cdot V = 0,$$

where ρ is fluid density, P is pressure, and μ is dynamic viscosity.

Symmetry boundary conditions were imposed for computations in the triangular area shown in Fig. 1 C as indicated. The astrocyte endfoot in the para-arterial space was modeled with two gaps (each 24-nm width) facing the triangular computational area (Fig. 1 C, left, inset). Solute concentrations were constant at the astrocyte endfoot gaps for advection–diffusion computations,

$$C_A = C_A{}^o, C_B = C_B{}^o,$$

and constant or pulsatile pressure boundary conditions were imposed for Navier–Stokes computations,

$$P_{in} = P_a \text{ or } P_{in} = P_a + P_{amp} \sin(2\pi t),$$

where C_o is solute concentration, P_a is pressure at the astrocyte endfoot gap in the para-arterial space, P_{amp} is amplitude of pulsatile pressure, and t is the time. Pulsatile pressure was modeled as a sinusoidal wave with frequency 1 Hz. Water transport through endfeet was computed as the sum of osmotic and hydrostatic pressure–driven fluxes,

$$J_v = Lp\ (RT \cdot \Delta Osm - \Delta P),$$

where J_v is total endfoot water flux, L_p is the hydraulic conductance, P_f is the osmotic water permeability coefficient (related by $P_f = (RT/v_w)L_p$), v_w is the partial molar volume of water, ΔP is the pressure difference, and ΔOsm is the osmolality difference through the endfeet. The endfeet and cells in the parenchyma are taken to be solute impermeable.

The astrocyte endfoot in the paravenous geometry was modeled to have two gaps (each 31-nm width; Fig. 1 C, right, inset). An advective flux boundary condition was imposed at the astrocyte endfoot gaps for advection–diffusion computations, which allows advective flux to exit the domain,

$$\nabla C_B = 0, \quad \nabla C_A = 0,$$

and zero-pressure boundary conditions were imposed for Navier–Stokes computations. Water transport through endfeet in the paravenous space was modeled as in the para-arterial space.

Stationary computations were also performed to obtain steady-state solutions, where the advective flux or zero-dye concentration ($C_B = 0$) boundary condi-

tions were imposed at the astrocyte endfoot in the paravenous space.

An HP Z600 workstation (12 Xeon E5645 CPUs and 32G RAM; Intel) was used for model computations, with 450,000–1,000,000 mesh elements. Fig. 1 C (left top, inset) shows the computational mesh density around the endfoot gap. The computation time was 1–12 h for kinetic computations and 5–30 min for steady-state computations.

Online supplemental material

Fig. S1 shows hydraulic conductance computation of the ECS model. Fig. S2 shows validation of advection–diffusion computation in one dimension in the absence of cell barriers. Fig. S3 shows comparison of predictions of a diffusion-only ($\Delta P = 0$) model with experimental data on solute accumulation in ECS. Fig. S4 shows comparison of predictions of a diffusion-only ($\Delta P = 0$) model for the current ECS geometry with experimental data on diffusion of 3-kD Texas red–dextran in the ECS. Fig. S5 shows convective fluid movement from para-arterial to paravenous spaces in brain ECS with an altered geometry of three arterioles and one venule. Fig. S6 shows convective fluid movement from para-arterial to paravenous spaces in brain ECS with altered geometry. Fig. S7 shows advective fluid movement through versus around astrocyte endfeet. Fig. S8 shows the influence of baseline mean pulsatile pressure in the para-arterial space on solute movement in brain ECS. Video 1 shows accumulation of solute B in the ECS for the absence of a pressure difference ($\Delta P = 0$, diffusion alone). Videos 2 and 3 show accumulation of solute B in the ECS for pressure difference $\Delta P = 1$ mmHg or $\Delta P = 10$ mmHg, respectively.

RESULTS

How large a hydrostatic pressure gradient is needed to drive advective flow in the ECS?

To demonstrate the general characteristics of model predictions, the advection–diffusion equations were solved with a constant, artificially imposed, para-arterial to paravenous pressure difference ($\Delta P = 1$ mmHg), an endfoot water permeability (P_f) of 0.04 cm/s, and a tracer solute diffusion coefficient ($D = 10^{-10}$ m^2/s) corresponding to that of an ∼10-kD macromolecule. After the establishment of a steady state in which all fluid compartments contained a single solute A (300 mM), tracer solute B (10 µM) was introduced into the para-arterial space and then entered and spread throughout the ECS by advection and diffusion (Fig. 2 A). Profiles of the concentration of solute B showed gradual filling of the entire ECS (Fig. 2 B, top). The pressure drop was dispersed into the entire ECS (Fig. 2 B, bottom), though it was nonlinear because of the convergent geometry with two arterioles feeding into one venule.

Control simulations were performed to confirm the validity of the computations; for one-dimensional geometry devoid of cellular structure in which the advection–diffusion equations can be solved analytically, the computed and analytical equations were in agreement (Fig. S2). For the two-dimensional computations as in Fig. 2 A, computed profiles changed by <1% for a fivefold increase in the density of the computational mesh, demonstrating that mesh density was adequate for accurate computations.

Normal intracranial pressure is ∼10 mmHg and varies by ∼1 mmHg during cardiac and respiratory cycles in the healthy human brain (Wagshul et al., 2011). These pressure cycles drive CSF flow in the low-resistance subarachnoid and ventricular compartments (Spector et al., 2015), but it remains unclear whether they are of sufficient magnitude to drive advective flow through the ECS as proposed by the glymphatic hypothesis. Steady-state pressure differences between the CSF and brain parenchyma are generally undetectable (<0.5 mmHg; Penn et al., 2005). We initially modeled a hypothetical constant pressure difference between the para-arterial and paravenous spaces; the accumulation of solute B in the ECS was computed in the absence of a pressure difference ($\Delta P = 0$, diffusion alone) and for ΔP of 1, 5, and 10 mmHg (Videos 1–3). The computations were performed with a moderately high water permeability of AQP4-containing astrocyte endfeet ($P_f = 0.04$ cm/s) and a solute diffusion coefficient of 10^{-10} m^2/s. Fig. 2 C shows concentration profiles of solute B in the ECS at time = 60 and 300 s (left) and its spatially integrated accumulation in the ECS (right, top). Diffusion alone gave half-filling time (equal to half-emptying time) of the ECS of ∼600 s, similar to the experimental time course observed for movement of a 3-kD tracer from the paravascular space into the parenchyma (from Fig. 2 in Iliff et al. [2012]; Fig. S3). The half-filling/emptying time was reduced by twofold with a para-arterial to paravenous pressure difference between 1 and 5 mmHg. ΣC_B is the area-integrated solute concentration, normalized to the steady-state solute concentration after the whole ECS area equilibrates at the para-arterial solute concentration (C_B^o). Fig. 2 C (right, bottom) shows that the steady-state transfer of solute B was approximately linear with the pressure difference, increasing by ∼2.5-fold for a 1-mmHg pressure difference.

Influence of ECS structure on convective solute transport

Changing the spatial distribution of Voronoi cells by using different initial sets of random numbers did not affect the computed accumulation of the tracer solute (Fig. 3 A). Decreasing the median ECS width from 60 to 45 nm slowed the rate of tracer accumulation slightly while increasing the median ECS width from 60 to 75 nm increased the rate slightly (Fig. 3 A,

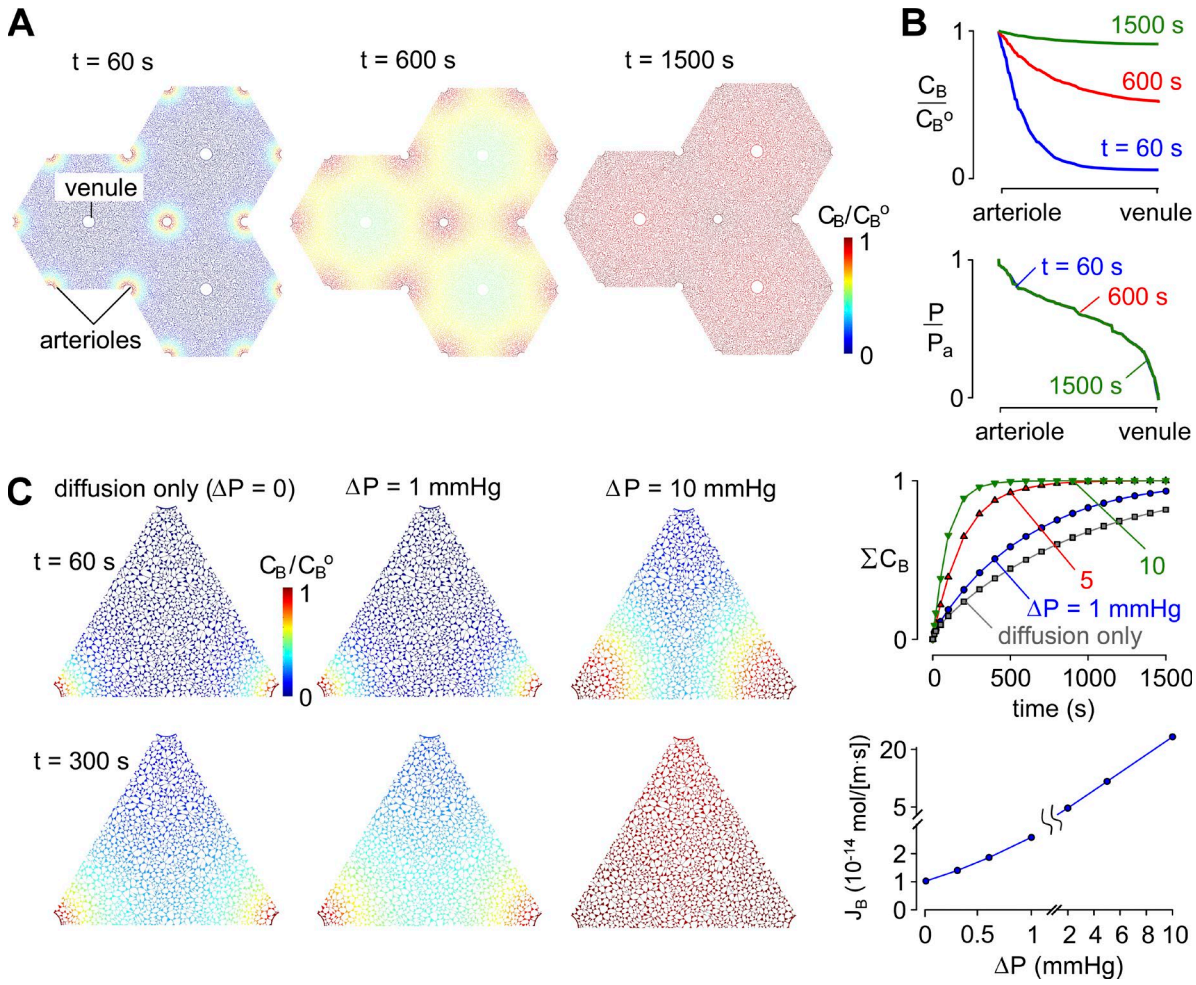

Figure 2. **General model predictions.** (A) Pseudocolored images showing tracer concentration (C_B/C_B^o) at time = 60, 600, and 1,500 s after a step increase in para-arterial tracer concentration for ΔP = 1 mmHg, P_f = 0.04 cm/s, and D = 10^{-10} m^2/s. (B) C_B/C_B^o and P/P_o profiles from para-arterial to paravenous space at the indicated times. (C, left) Pseudocolored images showing tracer solute accumulation in ECS after a step increase in para-arterial tracer concentration for para-arterial to paravenous pressure differences ΔP of 0 mmHg (diffusion alone) or 1 or 10 mmHg. Parameters: P_f = 0.04 cm/s and D = 10^{-10} m^2/s. (right, top) Kinetics of tracer solute accumulation in ECS for the indicated ΔP. (right, bottom) Steady-state tracer solute transfer from para-arterial to paravenous spaces for fixed concentration (C_B = 0) at the paravenous space.

right). Simulations of diffusion alone from a point source within the structure matched intensity distributions after tetramethylrhodamine injection into brain cortex (Thorne and Nicholson, 2006), demonstrating that the model accurately captured the diffusional tortuosity of brain (Fig. S4).

Changes in ECS volume fraction have been proposed to reduce convective flow through brain parenchyma during wakefulness (Xie et al., 2013). The sensitivity of convective solute transport to ECS volume fraction, α, was modeled. Fig. 3 B shows concentration profiles of solute B in the ECS at time = 600 s for the indicated ECS volume fractions, α = 0.1, 0.2, and 0.24 (0.24 is measured α in AQP4-null mouse brain) with ΔP = 1 mmHg, D = 10^{-10} m^2/s, and P_f = 0.04 cm/s. Fig. 3 B (right) shows the kinetics of accumulation of tracer solute B for the different α. Reducing ECS volume from α = 0.2 to 0.1 slowed the rate of accumulation of the solute tracer by ~30%, whereas increasing ECS from α = 0.2 to 0.24 increased the rate by ~40%.

The density of arterioles and venules shows substantial local variation within the primate cortex (Lauwers et al., 2008; Hirsch et al., 2012). We investigated the effect of altering the arteriolar density by increasing the number of arterioles (Fig. S5) and found that the rate of diffusional filling was somewhat increased compared with the original geometry. Conversely, decreasing the number of arterioles and increasing the distance between them by swapping the position of arterioles and venules in our model decreased the relative effectiveness of diffusional transport (Fig. S6). Intervascular distances in rodent cortex have been reported to be substantially smaller (~150 µm; Nguyen et al., 2011; Blinder et al., 2013) than those of the primate modeled

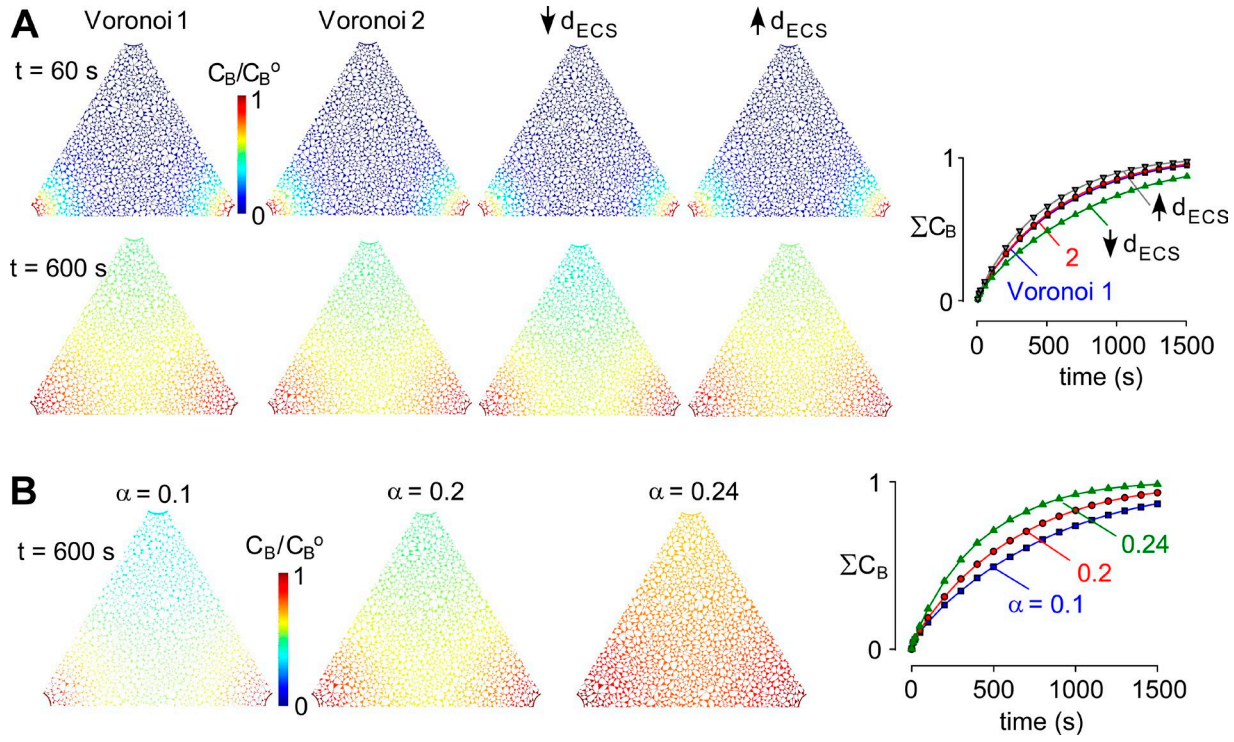

Figure 3. **Pressure dependence of solute movement in brain ECS.** (A) Influence of details of Voronoi cell geometry on model predictions. Four cell geometries were modeled: Voronoi 1 and 2, generated using different initial sets of random numbers with the same ECS width; Voronoi 3, with 25% reduced ECS width; and Voronoi 4, with 25% increased ECS width (each for the same ECS volume fraction). Images of $C_B/C_B°$ shown in the triangular computational domain at t = 60 and 600 s (left) and the kinetics of spatially integrated C_B in the ECS (ΣC_B; right). (B) Influence of ECS volume fraction, α. Computations as in A for ΔP = 1 mmHg, for the indicated α. (left) Pseudocolored images as in A. (right) Kinetics of tracer solute accumulation in ECS for the indicated α.

here, and therefore, paravascular tracers would accumulate even more rapidly by diffusion alone in this case.

Influence of solute size on ECS diffusive and advective transport

Transport of solutes into the brain is characterized by pronounced size-dependent differences in the rate of solute accumulation (Iliff et al., 2012). We determined how rapidly large and small solutes would enter the brain parenchyma under advective or diffusive conditions by performing simulations using tracer solute diffusion coefficients D of 0.2, 1, and 5×10^{-10} m^2/s, which covers the range expected for small solutes to macromolecules of molecular size ~200 kD. For these computations, ΔP was 0, 1, and 5 mmHg, with endfoot P_f of 0.04 cm/s. Fig. 4 A shows that for a 1-mmHg pressure difference, a fivefold increase in D from 0.2 to 10^{-10} m^2/s had little effect on solute accumulation in the ECS. Fig. 4 B summarizes the kinetics of solute accumulation for different ΔP. Solute accumulation is strongly dependent on D in the absence of advection (ΔP = 0) and becomes largely independent of D for substantial advection produced by ΔP = 5 mmHg. These results demonstrate that, as expected, significant advective flow is associated with faster accumulation of large solutes than would be expected from a purely diffusive mechanism. Comparison of these simulation results with experimental measurements of size-dependent tracer segregation from paravascular to parenchymal compartments might provide a sensitive assay of low-level advective transport in the parenchyma.

Does astrocyte foot process water permeability influence ECS solute transport?

In our simulations, the astrocyte endfoot was taken as single barrier with water permeability P_f (Fig. 1 C, insets). AQP4-M23 forms orthogonal arrays in astrocyte endfeet that typically occupy ~10% of the total area of the endfoot membrane and sometimes as much as 30% (Verbavatz et al., 1997; Rash et al., 1998; Smith et al., 2014). Given the unit water permeability of 2×10^{-13} cm^3/s of AQP4 monomers (Yang et al., 1997) and the 5–7-nm periodicity of AQP4 tetramers in orthogonal arrays (Landis and Reese, 1981), the unit water permeability of astrocyte endfoot membrane may be as high as 0.2–0.6 cm/s.

The effect of astrocyte endfoot water permeability, P_f, on ECS solute transport has been taken as evidence in support of the glymphatic mechanism (Iliff et al., 2012). Fig. 5 A (top) diagrams the hypothetical pressure-driven

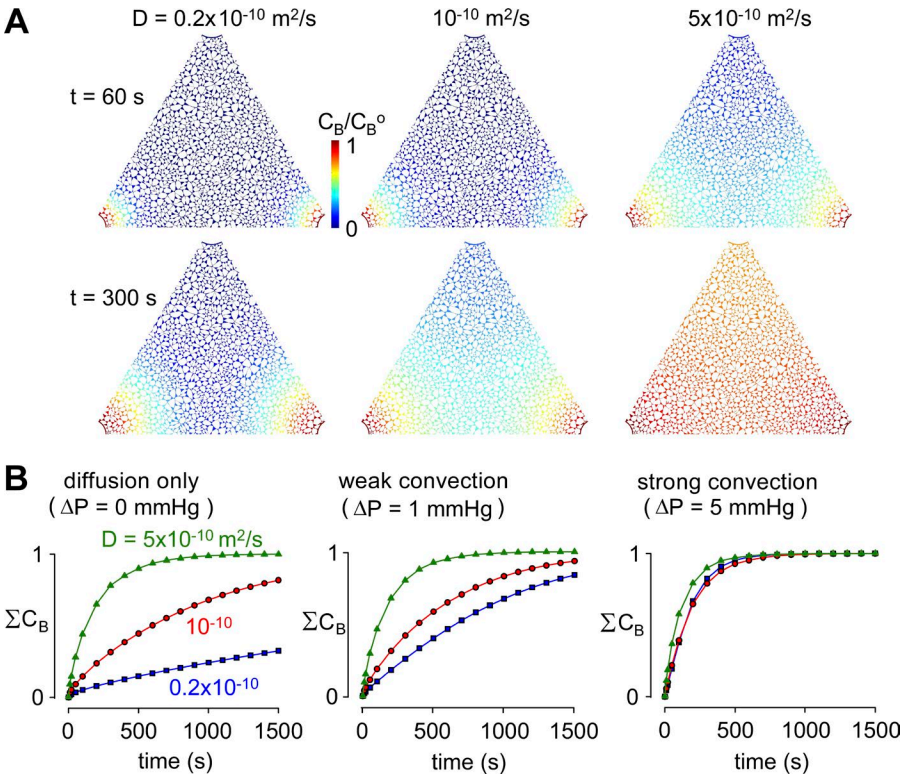

Figure 4. **Influence of tracer solute diffusion coefficient on solute movement in brain ECS.** (A) Pseudocolored images showing tracer solute accumulation in ECS, as in Fig 3, for the indicated tracer solute diffusion coefficients, D, and for ΔP = 1 mmHg. Parameters: P_f = 0.04 cm/s and α = 0.2. (B) Kinetics of tracer solute accumulation in ECS for the indicated D and ΔP.

advective flow through astrocyte endfeet, as well as osmotic water transport, with most water moving through AQP4. For simplicity, we modeled the endfoot as a single barrier containing AQP4, ignoring hydraulic resistance from the endfoot cytoplasm and the back membrane of the endfoot as well as the confounding osmotic effects of cytosolic dilution during water flow.

Solute accumulation in the ECS was computed for ΔP = 1 mmHg for astrocyte endfoot P_f of 0, 0.004, 0.04, and 0.4 cm/s, with D of 10^{-10} m^2/s. Fig. 5 A (bottom) shows pseudo-color images of solute B concentration at time = 60 and 600 s. There was no apparent effect of P_f from 0 to 0.4 cm/s on the kinetics of solute accumulation in the ECS or its transfer from para-arterial to paravenous spaces (Fig. 5 B, top). Conceptually, this result is not unexpected because pressure-driven advection is very inefficient compared with osmotically driven water transport. The insensitivity of ECS solute transport to P_f was also found for different parameter sets (Fig. 5 B, bottom), demonstrating the robustness of the conclusion. Computations with a more elaborate endfoot geometry that include the intracellular environment came to the same conclusion that trans-endfoot water flow is minimal (Fig. S7).

In considering additional factors that might confer an effect of endfoot P_f on solute accumulation in the ECS, we modeled solute transport in which ion pumping across astrocyte endfeet generates an osmotic gradient. An artificial ion flux was added to generate a small, 1 mOsm, or a very large, 25 mOsm, gradient across the astrocyte endfeet, with computations performed for P_f of 0, 0.004, and 0.04 cm/s, ΔP of 1 and 5 mmHg, and D of 10^{-10} m^2/s. As diagrammed in Fig. 5 C (top), ion pumping from the para-arterial space to the ECS, or in the opposite direction, creates an osmotic gradient that drives water transport across astrocyte endfeet, which alters pressure and osmolarity and hence pressure-driven fluid advection and diffusion through gaps in astrocyte endfeet. Fig. 5 C (bottom) shows pseudo-color images of the concentrations of solutes A and B at time = 600 s for ΔP = 1 mmHg, P_f of 0.04 cm/s, and D of 10^{-10} m^2/s. Ion pumping creates a concentration gradient of solute A (osmotic gradient) in the ECS (center), which does not significantly alter solute B concentration gradient (bottom). The kinetics of solute accumulation in the ECS was not altered by ion pumping for ΔP = 1 or 5 mmHg (Fig. 5 D).

Can pulsatile pressure in the para-arterial space drive parenchymal advection?

Though the experimental evidence suggests minimal or no steady-state pressure difference between CSF and ISF (interstitial fluid; Penn et al., 2005), there may be small pulsatile pressures in the para-arterial space produced by arterial pulsations (Bilston et al., 2003). We modeled the effect of a sinusoidal pressure pulsation in the para-arterial space with frequency 1 Hz, mean pressure 0 mmHg, and amplitudes of 0, 1, 5, and 100 mmHg (Fig. 6 A). Fig. 6 B shows pseudo-color images of solute B at time = 60 and 700 s for each pulsation amplitude.

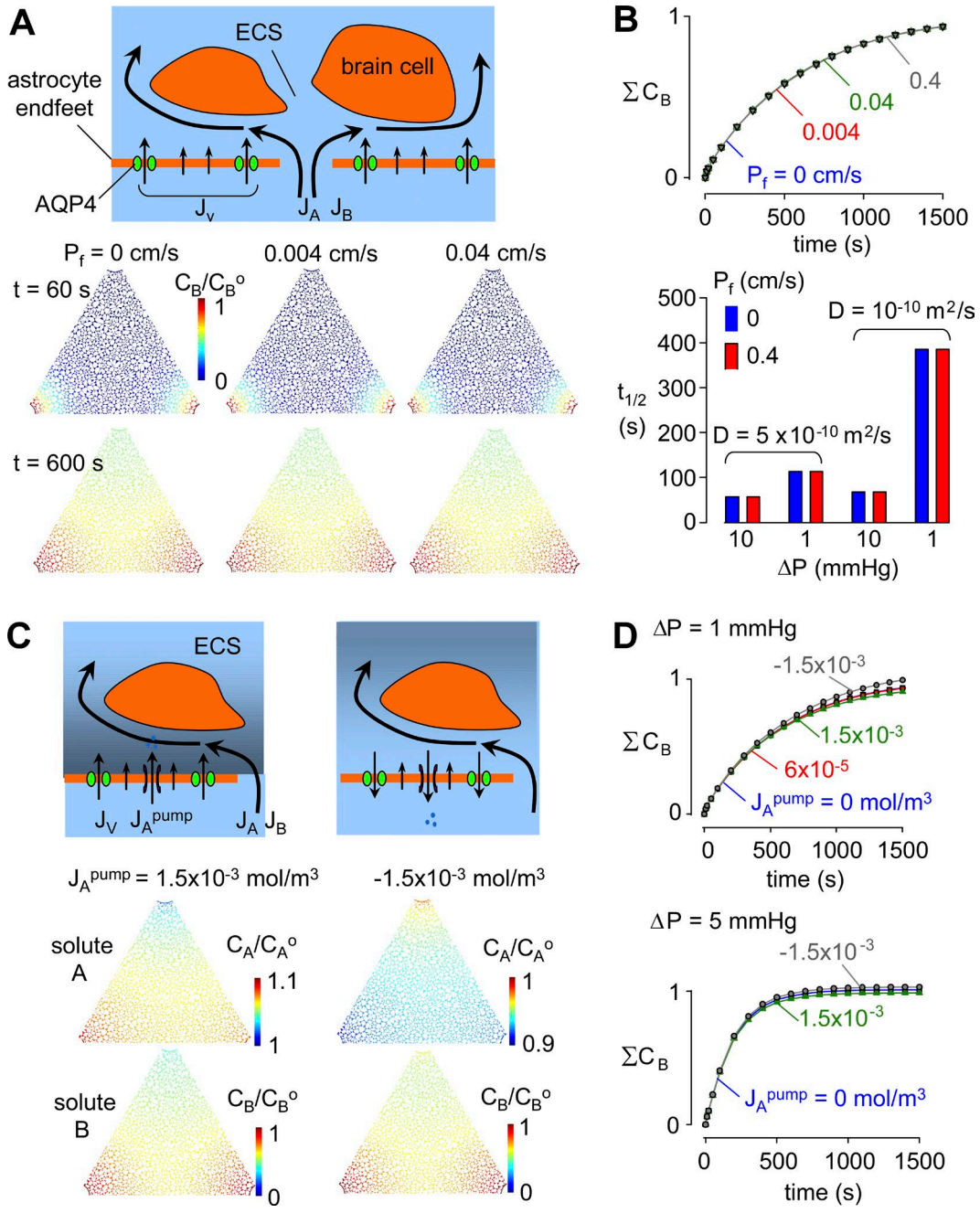

Figure 5. **Influence of astrocyte endfoot water permeability, P_f, on solute movement in brain ECS.** (A, top) Schematic showing hydrostatic and osmotic water transport across the astrocyte endfoot barrier and hydrostatic (advective) fluid movement in the gaps between endfeet. (bottom) Pseudocolored images showing tracer solute accumulation in ECS, as in Fig. 3, for P_f = 0, 0.004, and 0.04. For all computations in this figure, D = 10^{-10} m²/s and α = 0.2. (B, top) Kinetics of tracer solute accumulation in ECS for the indicated P_f. (bottom) Half-filling time for the indicated parameter sets. (C) Influence of active ion pumping to create an osmotic imbalance between the para-arterial space and ECS. (top) Schematic of possible effects of ion pumping into and out of the ECS across astrocyte endfeet, in which osmotically driven water transport across endfeet changes pressure in the ECS and hence the driving force for advective fluid movement from the para-arterial space into the ECS. (bottom) Pseudocolored images at time = 600 s for P_f = 0.04 cm/s showing accumulation of solutes A and B in ECS for the indicated active ion pumping flux, $J_A^{pump} = 1.5 \times 10^{-3}$ mol/m³ (active pumping into the ECS) and $J_A^{pump} = -1.5 \times 10^{-3}$ mol/m³ (pumping from the ECS). (D) Kinetics of tracer solute accumulation in ECS for ΔP = 1 and 5 mmHg.

Pulsatile pressures up to an amplitude of 5 mmHg did not change the kinetics of solute accumulation in the ECS (Fig. 6 C). We also tested an exceptionally high, nonphysiological amplitude of 100 mmHg to determine how large an amplitude is required to produce an effect (Fig. 6 C). A small increase in the rate of tracer

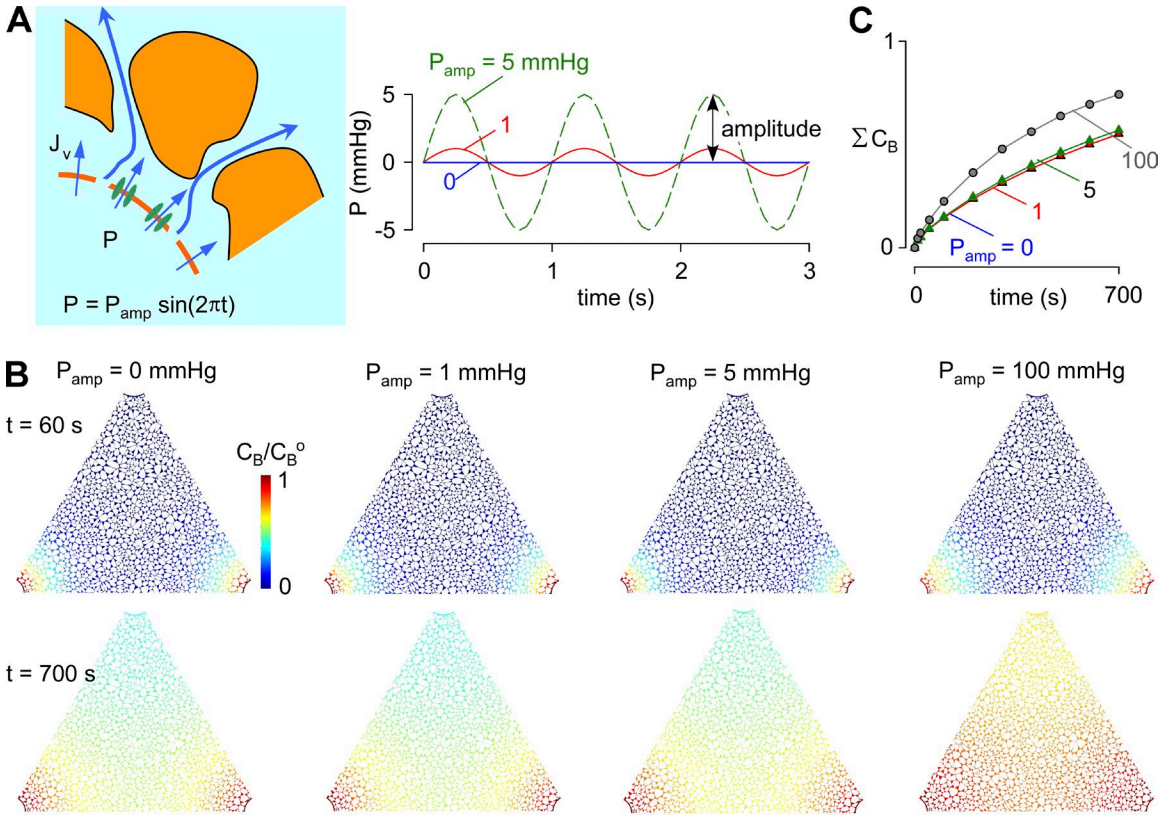

Figure 6. **Influence of pulsatile pressure in the para-arterial space on solute movement in brain ECS.** (A, left) Schematic showing hydrostatic pressure driven in the para-arterial space water transport across the astrocyte endfoot barrier; (right) para-arterial pressure waveform of amplitude P_{amp} and frequency 1 Hz. (B) Pseudocolored images showing tracer solute accumulation in the ECS, as in Fig 3, for different P_{amp}. Parameters: P_f = 0.04 cm/s, D = 10^{-10} m^2/s, and α = 0.2. (C) Kinetics of tracer solute accumulation in ECS for the indicated P_{amp}.

solute accumulation was found with the 100-mmHg amplitude. We also investigated the effect of the sinusoidal pulsatile pressure with nonzero baseline pressure difference. A 5-mmHg pulsatile pressure on top of a 1-mmHg mean pressure difference did not affect net transport, compared with a 1-mmHg pressure gradient in the absence of pulsation (Fig. S8).

DISCUSSION

The glymphatic mechanism proposes that hydrostatic, pressure-driven advective flow through brain parenchyma is responsible for solute clearance from the ECS. Advective flow represents a major departure from the conventional understanding of purely diffusive movement in the parenchyma, and it has been unclear what magnitude hydrostatic pressure difference would be needed to drive such a system and how it would respond to alterations in brain anatomy or physiology. Here, we applied computational fluid dynamics modeling to investigate the plausibility of advective fluid movement through brain parenchyma using physiologically realistic geometry and model parameters. Simulations in which hydrostatic pressure differences were applied between para-arterial and paravenous spaces predicted that (a) relatively high (>1 mmHg) steady-state pressure differences are needed to augment solute accumulation and clearance in brain parenchyma; (b) pulsatile hydrostatic pressure transients in the para-arterial space do not enhance solute transport; (c) changes in extracellular volume fraction may produce only minor changes in convective solute transport in the ECS; (d) advection preferentially accelerates transport of slowly diffusing molecules; and (e) water permeability of the perivascular glial sheath does not affect solute movement into the parenchyma. These findings differ from the predictions of a glymphatic mechanism, as (a) little or no advective solute transport is predicted to occur with physiological paravascular pressure differences; (b) AQP4-dependent water permeability of endfeet does not influence advective transport in the parenchyma; and (c) diffusive transport in ECS is sufficient to account quantitatively for experimental measurements of solute movement in the ECS.

The present model is based on a diagram reported by Iliff et al. (2012) that indicates a short-range clearance mechanism between descending arterioles and ascending venules in cortex. However, a long-range pathway

through the medial internal cerebral veins and the lateral ventral caudal rhinal veins was also proposed in the text of Iliff et al. (2012), though it was not described whether the proposed short- and long-range pathways are independent or combined, or how a solute can avoid the short-range pathway and reach distant veins. The long-range clearance pathway was not addressable using the present computation model because of limitations in computing power and information on long-range geometry. However, it is useful for qualitative analysis to consider simple scaling relations such as the Peclet number (Pe = UL/D), which is the ratio of the rate of advection by flow to the rate of diffusion, where U is the velocity, L is the characteristic length scale, and D is diffusion coefficient. For a long-range clearance pathway, a much higher pressure gradient is necessary to generate the same flow velocity even though the characteristic length scale increases (for example, from 250 µm to 1 or 2 mm). Thus, theoretical considerations would suggest that long-range parenchymal advection through gray matter is unlikely for physiologically plausible local pressure gradients, and it remains unclear what mechanism can account for the experimental observations of Iliff et al. (2012).

The hydrostatic pressure differences required to drive significant advective solute movement predicted by our model (>1 mmHg) are substantial when compared with typical intracranial pressures (7–15 mmHg). There are currently no experimental measurements of local hydrostatic pressure in paravascular compartments, but modeling studies suggest that pulsatile movement of the arterial wall can create fluctuations in hydrostatic pressure that might facilitate bi-directional mixing in the para-arterial space (Bilston et al., 2003; Schley et al., 2006; Wang and Olbricht, 2011). Iliff et al. (2013) proposed that arterial wall pulsations might also drive advective flow through the parenchyma. It remains unclear whether pulsatile fluid movement in the para-arterial space can create a net pressure difference between the para-arterial space and parenchyma. Alternative mechanisms, including gravity, electrodiffusion, and vasomotor contractions, may facilitate advective distribution of solutes in the paravascular space (Thrane et al., 2015), though it is unclear how these mechanisms could drive directional fluid transport as proposed by the glymphatic hypothesis.

Previous measurements of solute transport in the ECS have shown that movement of tracers in gray matter is generally well described by simple diffusion but have not ruled out the possibility of an advective component being important for movement of large macromolecules (Syková and Nicholson, 2008; Verkman, 2013). The modeling here confirmed that, as expected, significant advection would increase the movement of large molecules relative to small molecules through brain parenchyma. Experiments have generally observed the opposite, that large solutes move more slowly in vivo than would be predicted from in vitro diffusion measurements (Thorne and Nicholson, 2006; Zador et al., 2008), suggesting size-dependent constraints on diffusion through the parenchyma and an insignificant role for advection. It might be argued that classical measurements have not captured the contribution of advective flow, as craniotomy releases the pressure differences that drive this mechanism. Quantitative analysis of the distribution of coinjected tracers with a wide range of sizes might help to resolve whether there is a significant advective component to transport in the parenchyma.

Changes in the size of the ECS during sleep have been proposed to activate the glymphatic system to clear unwanted solutes from the ECS, offering a novel role for sleep (Xie et al., 2013). Our modeling suggests, however, that changes in extracellular volume fraction produce relatively modest effects on solute transport in the ECS. The relationship between hydraulic conductivity and aqueous fraction (porosity) is complex and strongly dependent on the microstructure of the porous substance under consideration. Existing models generally consider structures with overlapping barriers where small reductions in porosity can produce large reductions in conductivity caused by blockage of specific paths for solute flow, resulting in substantially increased hydraulic tortuosity (Koponen et al., 1996). This is not the case for brain parenchyma, where electrostatic repulsion between adjacent cell membranes prevents complete blockage of flow between cells as ECS volume fraction is decreased, which offers an explanation of the relative insensitivity of advective flow to changes in ECS volume fraction.

The glymphatic mechanism proposes that enrichment of AQP4 at endfeet is required for trans-astrocytic advective flow of water across the endfoot layer (Iliff et al., 2012) and that loss of polarization in reactive astrocytes prevents clearance of toxins from the parenchyma (Iliff et al., 2014). Problems with this proposed mechanism include the fact that AQP4 is only enriched at the perivascular membrane of endfeet and that cytosolic dilution creates osmotic gradients that oppose hydrostatic pressure-driven water flow (Smith et al., 2015). The modeling here showed no significant effect of endfoot water permeability over a wide range of parameter values. The experimental data of Iliff et al. (2012) showing greatly reduced movement of cisternally injected tracers into the brain in AQP4-null mice thus remains puzzling, particularly given the ∼20% increased baseline ECS volume fraction in AQP4-null mice (Yao et al., 2008), which is predicted to increase rather than reduce tracer accumulation in brain parenchyma.

Astrocyte endfeet and cell bodies in vivo are coupled by gap junctions to form a syncytium that may be involved in buffering transient local increases in specific solutes by diffusive and electro-diffusive transport.

Asgari et al. (2015) recently reported a model that attempted to resolve the inherent contradictions of the glymphatic hypothesis by postulating that a low-resistance intracellular pathway could provide an alternate route for a modest contribution of AQP4 to bulk flow in the parenchyma. Similar to our findings, they conclude that the water permeability of endfeet does not make an important contribution to advective flow from the paravascular to parenchymal space. Quantitative differences between our findings can be attributed to the choice of structural parameters, including an ECS width of 20 nm used by Asgari et al. (2015) (vs. 20–80 nm as discussed here) and an astrocyte process width of 500 nm, instead of the 50–200 nm as observed for fine astrocytic processes where gap junction coupling occurs (Lavialle et al., 2011); additionally, the one-dimensional model of Asgari et al. (2015) does not take into account the effect of solute dilution in creating an osmotic gradient that counters pressure-driven flow into cells, which is accounted for in the spatial model used here. We have not specifically addressed the relative importance of intracellular and extracellular advective flow deeper in the parenchyma where parenchymal AQP4 may play a role in diverting advective flow from the extracellular pathway through an astrocyte intracellular pathway (Asgari et al., 2015); however, we believe that similar geometric considerations may limit the importance of this pathway for pressure-driven advective flow. It remains possible that interactions between AQP4 and gap junction–coupled cells are important for redistribution of osmotic loads in the brain. The contradictory results generated by modeling and experiment suggest the need for further experimental investigation of the mechanisms underlying the proposed contribution of AQP4 to paravascular/parenchymal solute exchange.

Several limitations of our model are noted; first, diffusion and advection in brain ECS was modeled in two dimensions rather than three dimensions because of practical limitations on computational power. One of the limitations of a two-dimensional model is the reduction in degrees of freedom for fluid transport. In a three-dimensional model, the permeability may be slightly larger than in the two-dimensional model, as fluid has another dimension to escape tight obstacles. We have attempted to account for this by using a parenchymal structure chosen to closely approximate the likely resistance encountered to advective flow in a three-dimensional network of tunnels (Kinney et al., 2013). On a macroscopic level, we believe that a two-dimensional approximation is valid, as a single slice provides a reasonable approximation of the three-dimensional volume because of the perpendicular arrangement of arterioles and venules, within the cortex.

Second, the brain ECS boundaries defined by Voronoi cells were taken as noncompliant, which is justified because high pressure differences are required to produce small deformations in brain structure (Dutta-Roy et al., 2008). Third, we use an idealized arrangement of arterioles and venules in the parenchyma that might not capture the effects of local alterations in vascular density. Fourth, we have assumed that advection in the paravascular spaces is sufficient to effectively clamp solute concentrations in these regions, which may not be the case for the paravascular spaces surrounding small vessels where transport of water and solutes across endfeet could alter the composition of the paravascular fluid. Finally, the astrocyte endfeet were taken as single barriers with uniform water permeability, which could underestimate the actual hydraulic resistance of endfeet, though the computations performed using a wide range of P_f support the robustness of the conclusions. We have specifically modeled short-range convection between descending arterioles and ascending venules in the cortical brain parenchyma in this study, as suggested by the in vivo imaging experiments of Iliff et al. (2012). Advection clearly plays a role in long-range transport through the brain (Ichimura et al., 1991); however, this is generally assumed to be entirely through the paravascular spaces (Abbott, 2004) or along white matter tracts (Rosenberg et al., 1980). As mentioned in the second paragraph of the discussion, long-range, slow convection through parenchymal gray matter toward the deep cerebral veins seems unlikely based on theoretical concerns.

In summary, the modeling here does not support significant advective, glymphatic transport of solutes from the para-arterial space, through the parenchymal ECS, into the paravenous space. Our modeling supports the long-standing idea that diffusion is the primary determinant of solute movement in brain ECS under physiological conditions and that water permeability of astrocyte endfeet is the major determinant of osmotically driven, solute-free water transport into and out of the brain. Though significant advective transport in the parenchymal ECS is unlikely under physiological conditions according to the modeling, pressure-driven fluid advection, as occurs with convective drug delivery, can greatly enhance drug delivery to brain ECS, as suggested from the simulations in Fig. 2 C. Our findings thus mandate reexamination of the glymphatic mechanism and its implications in brain physiology and disease.

ACKNOWLEDGMENTS

Funding sources: National Institutes of Health grants EB00415, EY13574, DK72517, DK35124, and DK101273, and a grant from the Guthy-Jackson Charitable Foundation.

The authors declare no competing financial interests.

Author contributions: B.-J. Jin, A.J. Smith, and A.S. Verkman designed research. B.-J. Jin and A.J. Smith performed research. B.-J. Jin, A.J. Smith, and A.S. Verkman analyzed data. B.-J. Jin, A.J. Smith, and A.S. Verkman wrote the paper.

José D. Faraldo-Gómez served as editor.

Submitted: 30 August 2016
Accepted: 21 October 2016

REFERENCES

Abbott, N.J. 2004. Evidence for bulk flow of brain interstitial fluid: significance for physiology and pathology. *Neurochem. Int.* 45:545–552. http://dx.doi.org/10.1016/j.neuint.2003.11.006

Adams, D.L., V. Piserchia, J.R. Economides, and J.C. Horton. 2015. Vascular supply of the cerebral cortex is specialized for cell layers but not columns. *Cereb. Cortex.* 25:3673–3681. http://dx.doi.org/10.1093/cercor/bhu221

Asgari, M., D. de Zélicourt, and V. Kurtcuoglu. 2015. How astrocyte networks may contribute to cerebral metabolite clearance. *Sci. Rep.* 5:15024. http://dx.doi.org/10.1038/srep15024

Basser, P.J. 1992. Interstitial pressure, volume, and flow during infusion into brain tissue. *Microvasc. Res.* 44:143–165. http://dx.doi.org/10.1016/0026-2862(92)90077-3

Bilston, L.E., D.F. Fletcher, A.R. Brodbelt, and M.A. Stoodley. 2003. Arterial pulsation-driven cerebrospinal fluid flow in the perivascular space: a computational model. *Comput. Methods Biomech. Biomed. Engin.* 6:235–241. http://dx.doi.org/10.1080/10255840310001606116

Binder, D.K., M.C. Papadopoulos, P.M. Haggie, and A.S. Verkman. 2004. In vivo measurement of brain extracellular space diffusion by cortical surface photobleaching. *J. Neurosci.* 24:8049–8056. http://dx.doi.org/10.1523/JNEUROSCI.2294-04.2004

Blinder, P., P.S. Tsai, J.P. Kaufhold, P.M. Knutsen, H. Suhl, and D. Kleinfeld. 2013. The cortical angiome: an interconnected vascular network with noncolumnar patterns of blood flow. *Nat. Neurosci.* 16:889–897. http://dx.doi.org/10.1038/nn.3426

Coloma, M., J.D. Schaffer, R.O. Carare, P.R. Chiarot, and P. Huang. 2016. Pulsations with reflected boundary waves: a hydrodynamic reverse transport mechanism for perivascular drainage in the brain. *J. Math. Biol.* 73:469–490. http://dx.doi.org/10.1007/s00285-015-0960-6

Dutta-Roy, T., A. Wittek, and K. Miller. 2008. Biomechanical modelling of normal pressure hydrocephalus. *J. Biomech.* 41:2263–2271. http://dx.doi.org/10.1016/j.jbiomech.2008.04.014

Goodman, J.A., C.D. Kroenke, G.L. Bretthorst, J.J.H. Ackerman, and J.J. Neil. 2005. Sodium ion apparent diffusion coefficient in living rat brain. *Magn. Reson. Med.* 53:1040–1045. http://dx.doi.org/10.1002/mrm.20444

Hirsch, S., J. Reichold, M. Schneider, G. Székely, and B. Weber. 2012. Topology and hemodynamics of the cortical cerebrovascular system. *J. Cereb. Blood Flow Metab.* 32:952–967. http://dx.doi.org/10.1038/jcbfm.2012.39

Hladky, S.B., and M.A. Barrand. 2014. Mechanisms of fluid movement into, through and out of the brain: evaluation of the evidence. *Fluids Barriers CNS.* 11:26. http://dx.doi.org/10.1186/2045-8118-11-26

Hrabe, J., S. Hrabetová, and K. Segeth. 2004. A model of effective diffusion and tortuosity in the extracellular space of the brain. *Biophys. J.* 87:1606–1617. http://dx.doi.org/10.1529/biophysj.103.039495

Ichimura, T., P.A. Fraser, and H.F. Cserr. 1991. Distribution of extracellular tracers in perivascular spaces of the rat brain. *Brain Res.* 545:103–113. http://dx.doi.org/10.1016/0006-8993(91)91275-6

Iliff, J.J., M. Wang, Y. Liao, B.A. Plogg, W. Peng, G.A. Gundersen, H. Benveniste, G.E. Vates, R. Deane, S.A. Goldman, et al. 2012. A paravascular pathway facilitates CSF flow through the brain parenchyma and the clearance of interstitial solutes, including amyloid β. *Sci. Transl. Med.* 4:147ra111. http://dx.doi.org/10.1126/scitranslmed.3003748

Iliff, J.J., M. Wang, D.M. Zeppenfeld, A. Venkataraman, B.A. Plog, Y. Liao, R. Deane, and M. Nedergaard. 2013. Cerebral arterial pulsation drives paravascular CSF-interstitial fluid exchange in the murine brain. *J. Neurosci.* 33:18190–18199. http://dx.doi.org/10.1523/JNEUROSCI.1592-13.2013

Iliff, J.J., M.J. Chen, B.A. Plog, D.M. Zeppenfeld, M. Soltero, L. Yang, I. Singh, R. Deane, and M. Nedergaard. 2014. Impairment of glymphatic pathway function promotes tau pathology after traumatic brain injury. *J. Neurosci.* 34:16180–16193. http://dx.doi.org/10.1523/JNEUROSCI.3020-14.2014

Jessen, N.A., A.S. Munk, I. Lundgaard, and M. Nedergaard. 2015. The glymphatic system: A beginner's guide. *Neurochem. Res.* 40:2583–2599. http://dx.doi.org/10.1007/s11064-015-1581-6

Jin, S., Z. Zador, and A.S. Verkman. 2008. Random-walk model of diffusion in three dimensions in brain extracellular space: comparison with microfiberoptic photobleaching measurements. *Biophys. J.* 95:1785–1794. http://dx.doi.org/10.1529/biophysj.108.131466

Kaczmarek, M., R.P. Subramaniam, and S.R. Neff. 1997. The hydromechanics of hydrocephalus: steady-state solutions for cylindrical geometry. *Bull. Math. Biol.* 59:295–323. http://dx.doi.org/10.1007/BF02462005

Kinney, J.P., J. Spacek, T.M. Bartol, C.L. Bajaj, K.M. Harris, and T.J. Sejnowski. 2013. Extracellular sheets and tunnels modulate glutamate diffusion in hippocampal neuropil. *J. Comp. Neurol.* 521:448–464. http://dx.doi.org/10.1002/cne.23181

Koponen, A., M. Kataja, and J. Timonen. 1996. Tortuous flow in porous media. *Phys. Rev. E Stat. Phys. Plasmas Fluids Relat. Interdiscip. Topics.* 54:406–410.

Landis, D.M., and T.S. Reese. 1981. Astrocyte membrane structure: changes after circulatory arrest. *J. Cell Biol.* 88:660–663. http://dx.doi.org/10.1083/jcb.88.3.660

Lauwers, F., F. Cassot, V. Lauwers-Cances, P. Puwanarajah, and H. Duvernoy. 2008. Morphometry of the human cerebral cortex microcirculation: general characteristics and space-related profiles. *Neuroimage.* 39:936–948. http://dx.doi.org/10.1016/j.neuroimage.2007.09.024

Lavialle, M., G. Aumann, E. Anlauf, F. Pröls, M. Arpin, and A. Derouiche. 2011. Structural plasticity of perisynaptic astrocyte processes involves ezrin and metabotropic glutamate receptors. *Proc. Natl. Acad. Sci. USA.* 108:12915–12919. http://dx.doi.org/10.1073/pnas.1100957108

Mathiisen, T.M., K.P. Lehre, N.C. Danbolt, and O.P. Ottersen. 2010. The perivascular astroglial sheath provides a complete covering of the brain microvessels: an electron microscopic 3D reconstruction. *Glia.* 58:1094–1103. http://dx.doi.org/10.1002/glia.20990

Nguyen, J., N. Nishimura, R.N. Fetcho, C. Iadecola, and C.B. Schaffer. 2011. Occlusion of cortical ascending venules causes blood flow decreases, reversals in flow direction, and vessel dilation in upstream capillaries. *J. Cereb. Blood Flow Metab.* 31:2243–2254. http://dx.doi.org/10.1038/jcbfm.2011.95

Papadopoulos, M.C., J.K. Kim, and A.S. Verkman. 2005. Extracellular space diffusion in central nervous system: anisotropic diffusion measured by elliptical surface photobleaching. *Biophys. J.* 89:3660–3668. http://dx.doi.org/10.1529/biophysj.105.068114

Penn, R.D., M.C. Lee, A.A. Linninger, K. Miesel, S.N. Lu, and L. Stylos. 2005. Pressure gradients in the brain in an experimental model of hydrocephalus. *J. Neurosurg.* 102:1069–1075. http://dx.doi.org/10.3171/jns.2005.102.6.1069

Rash, J.E., T. Yasumura, C.S. Hudson, P. Agre, and S. Nielsen. 1998. Direct immunogold labeling of aquaporin-4 in square arrays of astrocyte and ependymocyte plasma membranes in rat brain and spinal cord. *Proc. Natl. Acad. Sci. USA.* 95:11981–11986. http://dx.doi.org/10.1073/pnas.95.20.11981

Rosenberg, G.A., W.T. Kyner, and E. Estrada. 1980. Bulk flow of brain interstitial fluid under normal and hyperosmolar conditions. *Am. J. Physiol.* 238:F42–F49.

Schley, D., R. Carare-Nnadi, C.P. Please, V.H. Perry, and R.O. Weller. 2006. Mechanisms to explain the reverse perivascular transport of solutes out of the brain. *J. Theor. Biol.* 238:962–974. http://dx.doi.org/10.1016/j.jtbi.2005.07.005

Smith, A.J., B.J. Jin, J. Ratelade, and A.S. Verkman. 2014. Aggregation state determines the localization and function of M1- and M23-aquaporin-4 in astrocytes. *J. Cell Biol.* 204:559–573. http://dx.doi.org/10.1083/jcb.201308118

Smith, A.J., B.J. Jin, and A.S. Verkman. 2015. Muddying the water in brain edema? *Trends Neurosci.* 38:331–332. http://dx.doi.org/10.1016/j.tins.2015.04.006

Spector, R., S. Robert Snodgrass, and C.E. Johanson. 2015. A balanced view of the cerebrospinal fluid composition and functions: Focus on adult humans. *Exp. Neurol.* 273:57–68. http://dx.doi.org/10.1016/j.expneurol.2015.07.027

Syková, E., and C. Nicholson. 2008. Diffusion in brain extracellular space. *Physiol. Rev.* 88:1277–1340. http://dx.doi.org/10.1152/physrev.00027.2007

Thorne, R.G., and C. Nicholson. 2006. In vivo diffusion analysis with quantum dots and dextrans predicts the width of brain extracellular space. *Proc. Natl. Acad. Sci. USA.* 103:5567–5572. http://dx.doi.org/10.1073/pnas.0509425103

Thrane, A.S., V. Rangroo Thrane, B.A. Plog, and M. Nedergaard. 2015. Filtering the muddied waters of brain edema. *Trends Neurosci.* 38:333–335. http://dx.doi.org/10.1016/j.tins.2015.04.009

Verbavatz, J.M., T. Ma, R. Gobin, and A.S. Verkman. 1997. Absence of orthogonal arrays in kidney, brain and muscle from transgenic knockout mice lacking water channel aquaporin-4. *J. Cell Sci.* 110:2855–2860.

Verkman, A.S. 2013. Diffusion in the extracellular space in brain and tumors. *Phys. Biol.* 10:045003. http://dx.doi.org/10.1088/1478-3975/10/4/045003

Wagshul, M.E., P.K. Eide, and J.R. Madsen. 2011. The pulsating brain: A review of experimental and clinical studies of intracranial pulsatility. *Fluids Barriers CNS.* 8:5. http://dx.doi.org/10.1186/2045-8118-8-5

Wang, P., and W.L. Olbricht. 2011. Fluid mechanics in the perivascular space. *J. Theor. Biol.* 274:52–57. http://dx.doi.org/10.1016/j.jtbi.2011.01.014

Weller, R.O., H.Y. Yow, S.D. Preston, I. Mazanti, and J.A. Nicoll. 2002. Cerebrovascular disease is a major factor in the failure of elimination of Aβ from the aging human brain: Implications for therapy of Alzheimer's disease. *Ann. N. Y. Acad. Sci.* 977:162–168. http://dx.doi.org/10.1111/j.1749-6632.2002.tb04812.x

Wolak, D.J., and R.G. Thorne. 2013. Diffusion of macromolecules in the brain: implications for drug delivery. *Mol. Pharm.* 10:1492–1504. http://dx.doi.org/10.1021/mp300495e

Xie, L., H. Kang, Q. Xu, M.J. Chen, Y. Liao, M. Thiyagarajan, J. O'Donnell, D.J. Christensen, C. Nicholson, J.J. Iliff, et al. 2013. Sleep drives metabolite clearance from the adult brain. *Science.* 342:373–377. http://dx.doi.org/10.1126/science.1241224

Yang, B., A.N. van Hoek, and A.S. Verkman. 1997. Very high single channel water permeability of aquaporin-4 in baculovirus-infected insect cells and liposomes reconstituted with purified aquaporin-4. *Biochemistry.* 36:7625–7632. http://dx.doi.org/10.1021/bi970231r

Yao, X., S. Hrabetová, C. Nicholson, and G.T. Manley. 2008. Aquaporin-4-deficient mice have increased extracellular space without tortuosity change. *J. Neurosci.* 28:5460–5464. http://dx.doi.org/10.1523/JNEUROSCI.0257-08.2008

Zador, Z., M. Magzoub, S. Jin, G.T. Manley, M.C. Papadopoulos, and A.S. Verkman. 2008. Microfiberoptic fluorescence photobleaching reveals size-dependent macromolecule diffusion in extracellular space deep in brain. *FASEB J.* 22:870–879. http://dx.doi.org/10.1096/fj.07-9468com